2020

Cryo-EM structures of the air-oxidized and dithionite-reduced photosynthetic alternative complex III from Roseiflexus castenholzii

Yang Shi
University of Chinese Academy of Sciences

Yueyong Xin
Hangzhou Normal University

Chao Wang
Hangzhou Normal University

Robert E Blankenship
Washington University School of Medicine in St. Louis

Fei Sun
University of Chinese Academy of Sciences

See next page for additional authors

STRUCTURAL BIOLOGY

Cryo-EM structures of the air-oxidized and dithionite-reduced photosynthetic alternative complex III from *Roseiflexus castenholzii*

Yang Shi[1,2]*, Yueyong Xin[3,4]*, Chao Wang[3]*, Robert E. Blankenship[5], Fei Sun[1,2,6]†, Xiaoling Xu[3,4,7]†

Alternative complex III (ACIII) is a multisubunit quinol:electron acceptor oxidoreductase that couples quinol oxidation with transmembrane proton translocation in both the respiratory and photosynthetic electron transport chains of bacteria. The coupling mechanism, however, is poorly understood. Here, we report the cryo-EM structures of air-oxidized and dithionite-reduced ACIII from the photosynthetic bacterium *Roseiflexus castenholzii* at 3.3- and 3.5-Å resolution, respectively. We identified a menaquinol binding pocket and an electron transfer wire comprising six hemes and four iron-sulfur clusters that is capable of transferring electrons to periplasmic acceptors. We detected a proton translocation passage in which three strictly conserved, mid-passage residues are likely essential for coupling the redox-driven proton translocation across the membrane. These results allow us to propose a previously unrecognized coupling mechanism that links the respiratory and photosynthetic functions of ACIII. This study provides a structural basis for further investigation of the energy transformation mechanisms in bacterial photosynthesis and respiration.

INTRODUCTION

Photosynthesis transforms solar energy to chemical energy and supports nearly all life on Earth. Sunlight is absorbed by pigments in the light-harvesting (LH) antenna system, and excitation energy is transferred to the reaction center (RC), where photochemistry occurs, initiating an electron transfer process. The electron transport chain (ETC) couples the redox reactions associated with electron donors and acceptors to proton translocation to build up a proton motive force across the membrane, which, in turn, drives the formation of adenosine triphosphate (ATP) and other energy-consuming processes. In photosynthetic and respiratory ETCs, complex III (mitochondrial and bacterial cytochrome bc_1, chloroplast and cyanobacterial cytochrome b_6f) functions primarily to couple thermodynamically favorable electron transfer to proton translocation across the membrane (*1*–*3*). As quinol:electron acceptor oxidoreductases, these complexes create a transmembrane (TM) proton gradient through the Q-cycle mechanism: Four protons are translocated for every two electrons transferred to cytochrome c (cyt c) or plastocyanin upon quinol oxidation (*3*–*5*).

Notably, a functional counterpart for the cyt bc_1 complex, alternative complex III (ACIII), has been identified in a wide range of bacterial taxa, and its presence usually coincides with the absence of the cyt bc_1 complex (*6*–*10*). This complex is structurally and compositionally unrelated to the bacterial cyt bc_1 complex, but it plays the same central role as a quinol:electron acceptor oxidoreductase in both the respiratory and photosynthetic ETCs (*6*, *8*–*13*). In the respiratory chain, ACIII is usually associated with different cyt c oxidases and functions in aerobic electron transfer (*14*, *15*). In the photosynthetic ETC of *Chloroflexus aurantiacus*, in which ACIII was originally discovered (*16*), the photosynthetic ACIII catalyzes the oxidation of menaquinol and mediates transfer of the released electrons to a periplasmic blue copper protein auracyanin, which, in turn, completes a cyclic electron transfer back to the RC (*9*, *12*, *13*).

Recent studies of the respiratory ACIII from *Rhodothermus marinus (17)* and *Flavobacterium johnsoniae (18)* have elucidated the structural features of this complex that are related to quinol coordination, cyt c oxidase association, and putative proton translocation. Regarding the association with different cyt c oxidases and the linear electron transfer mode of respiratory ACIII, the photosynthetic ACIII has a distinct composition and functions in a simple and efficient cyclic ETC using the electron donor menaquinol (*8*, *12*, *13*, *19*, *20*). However, the structure of the photosynthetic ACIII remains unknown. In particular, the fundamental coupling mechanisms underlying the menaquinol oxidation and proton translocation of the respiratory and photosynthetic ACIII complexes have received little research attention. Therefore, a structural investigation of the photosynthetic ACIII is necessary for a deeper understanding of the common coupling mechanism used by the ACIII from diverse bacterial taxa.

Roseiflexus castenholzii is a chlorosome-less filamentous anoxygenic phototroph. It contains a mosaic LH antenna, the type II pheophytin-quinone RC, and a cyclic electron transport system. The LH antenna of *R. castenholzii* is structurally similar to the LH1, but spectroscopically it resembles the LH2 of purple bacteria (*19*, *21*, *22*). Our previous structure of the *R. castenholzii* core complex (*rc*RC-LH) revealed a previously unknown architecture and a new type of menaquinone shuttling channel in the bacterial RC-LHs and illustrated the molecular basis underlying the LH and energy transfer mechanisms of early prokaryotes (*23*). We then extracted and purified *R. castenholzii* ACIII and its periplasmic electron acceptor auracyanin and revealed that ACIII oxidizes menaquinol-4 or menaquinol-7

[1]National Laboratory of Biomacromolecules, National Center of Protein Science-Beijing, CAS Center for Excellence in Biomacromolecules, Institute of Biophysics, Chinese Academy of Sciences, Beijing 100101, China. [2]University of Chinese Academy of Sciences, Beijing 100049, China. [3]Hangzhou Normal University, 2318 Yuhangtang Road, Cangqian, Yuhang District, Hangzhou 311121, Zhejiang Province, China. [4]Photosynthesis Research Center, College of Life and Environmental Sciences, Hangzhou Normal University, Hangzhou 311121, Zhejiang, China [5]Departments of Biology and Chemistry, Washington University in St. Louis, St. Louis, MO 63130, USA. [6]Center for Biological Imaging, Institute of Biophysics, Chinese Academy of Sciences, Beijing 100101, China. [7]Key Laboratory of Aging and Cancer Biology of Zhejiang Province, School of Medicine and The Affiliated Hospital, Hangzhou Normal University, Hangzhou 311121, Zhejiang, China.
*These authors contributed equally to this work.
†Corresponding author. Email: xuxl@hznu.edu.cn (X.X.); feisun@ibp.ac.cn (F.S.)

and transfers the electrons to the copper ion coordinated in auracyanin (*24*). Here, we report the structures of the six-subunit *R. castenholzii* ACIII in air-oxidized and dithionite-reduced states, determined by single-particle cryo–electron microscopy (cryo-EM) at 3.3- and 3.5-Å resolution, respectively. We elucidated its structural features and here propose a previously unrecognized redox-coupled electron transfer and proton translocation mechanism that apparently links the respiratory and photosynthetic functions of the ACIII.

RESULTS

Composition and overall structure

We purified the ACIII from phototrophically grown *R. castenholzii* using a modification of previous methods (*7*, *8*, *16*). We next used SDS–polyacrylamide gel electrophoresis (PAGE) and blue native PAGE to evaluate the purified ACIII (fig. S1A). Consistent with the molecular size expected from the corresponding gene sequences, we observed that the overall 300-kDa complex was composed of six subunits (ActA, ActB, ActC, ActD, ActE, and ActF), with molecular masses ranging from ~10 to 110 kDa (fig. S1A). Each subunit was confirmed by peptide mass fingerprinting (PMF) (tables S1 and S2). Further, gel filtration analysis (fig. S1B) indicated that the purified ACIII was a monomer containing one copy of each subunit. Spectral analysis indicated that the purified ACIII was air-oxidized: It was reduced via addition of sodium dithionite (fig. S1C). The reduced-minus-oxidized difference spectrum showed two absorbance peaks at 524 and 554 nm, indicating the increase of the c-type heme absorbance after reduction (fig. S1D).

To elucidate the proposed conformational changes that were involved in the redox-driven proton translocation of respiratory ACIII (*17*), the vitrified air-oxidized and dithionite-reduced ACIII were individually subjected to cryo-EM single-particle analysis. A dataset of 257,815 particles of the air-oxidized ACIII was used to reconstruct an electron potential map with an average resolution of 3.3 Å and a local resolution extending to 2.5 Å (fig. S2 and movie S1). The final reconstructed cryo-EM map was resolved and enabled us to build an accurate model of the TM helices with side chains in the air-oxidized ACIII (fig. S3) and all the cofactors and lipid molecules (Table 1 and fig. S4). The cryo-EM map of the dithionite-reduced ACIII was reconstructed from 488,581 particles to 3.5-Å resolution, the composition and overall structure of which resembles that of the air-oxidized ACIII (Table 1, fig. S5, and movie S2).

Different from the respiratory ACIII from *R. marinus* that contains seven subunits (ActABCDEFH) and one additional unidentified subunit (*17*), the photosynthetic ACIII only contains six core subunits (ActA, ActB, ActC, ActD, ActE, and ActF) as in *F. johnsoniae (18)*. Superimposition of *R. castenholzii* ACIII structure with that of *R. marinus* and *F. johnsoniae* gives a main-chain root mean square deviation (RMSD) of 1.5 and 3.2 Å, respectively. Like the two respiratory ACIII structures, *R. castenholzii* ACIII is assembled into an "L"-shaped architecture with dimensions of 141 by 98 by 80 Å; a TM arm (42 Å) containing 23 TM helices from subunits ActA, ActC, ActD, and ActF; and a peripheral arm comprising the periplasmic subunits ActA, ActB, and ActE. On the periplasmic side, subunit ActB forms extensive contacts with ActE, the penta-heme binding domain of ActA, and the periplasmic region of ActC, ActD, and ActF. The loop between the two TMs of ActD inserts into the interface of ActA, ActB, ActC, and ActF. The globular domain of ActD is located in the cytoplasm (Fig. 1, A and B).

Table 1. Data collection, processing, and refinement statistics.

	Air-oxidized ACIII (EMDB-0937) (PDB 6LOE)	Dithionite-reduced ACIII (EMDB-0936) (PDB 6LOD)
Data collection and processing		
Magnification	22,500	22,500
Voltage (kV)	300	300
Electron exposure (e^-/Å2)	59	60
Defocus range (μm)	1.2–3.3	1.0–3.0
Pixel size (Å)	1.04	1.04
Symmetry imposed	C1	C1
Initial particle images (no.)	257,815	488,581
Final particle images (no.)	177,489	207,633
Map resolution (Å)	3.2	3.5
FSC threshold	0.143	0.143
Refinement		
Model resolution (Å)	3.3	3.5
FSC threshold	0.5	0.5
Map sharpening *B* factor (Å^2)	−125	−135
Model composition		
Nonhydrogen atoms	19,024	19,024
Protein residues	2,329	2,329
Ligands	17	17
RMSDs		
Bond lengths (Å)	0.025	0.025
Bond angles (°)	1.548	1.420
Validation		
MolProbity score	1.95	2.20
Clashscore	8.57	14.09
Poor rotamers (%)	0.42	0.21
Ramachandran plot		
Favored (%)	91.84	90.03
Allowed (%)	8.16	9.97
Disallowed (%)	0.00	0.00

Similar to *R. marinus* ACIII, given its known electron transport function, one [3Fe-4S] and three [4Fe-4S] clusters in ActB, and six c-type hemes (five in ActA and one in ActE) were modeled in the density map of *R. castenholzii* ACIII (Fig. 1C and fig. S4), apparently forming wires of the six hemes and the iron-sulfur clusters (Fig. 1D). The six c-type hemes exemplify identical positions and orientations as that in *R. marinus* and *F. johnsoniae* ACIII, but there are only one [3Fe-4S] cluster and one [4Fe-4S] cluster identified at deviated positions in *F. johnsoniae* ACIII (fig. S6A). The six hemes and four iron-sulfur clusters are all located within reasonable edge-to-edge

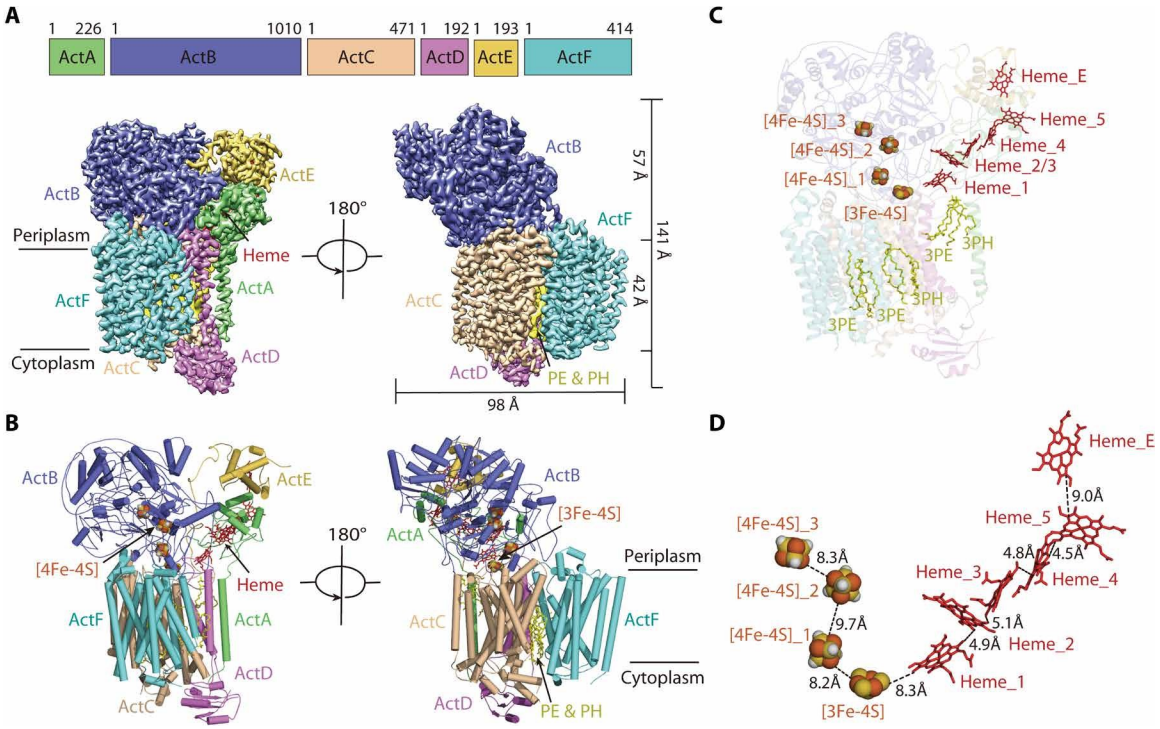

Fig. 1. Overall structure of the photosynthetic ACIII from R. castenholzii**.** (**A**) The cryo-EM map of the air-oxidized ACIII is shown from the front (left) and back (right) view and represented with the dimensions of the TM and periplasmic region. Each of the six subunits is labeled with the length of its encoded amino acid. (**B**) Cartoon representation of the air-oxidized ACIII. The c-type hemes and lipids are shown as sticks, and the iron-sulfur clusters are shown as spheres. (**C**) Representation of the arrangement of cofactors in the air-oxidized ACIII. (**D**) Edge-to-edge distance between the iron-sulfur clusters and the hemes in the air-oxidized ACIII. The distances are labeled and shown in dashed lines. Color codes for all panels: lime green, ActA; slate, ActB; wheat, ActC; violet, ActD; yellow orange, ActE; aquamarine, ActF; red, c-type heme; orange brown, iron-sulfur clusters; yellow, lipids.

distances (less than 14 Å) to permit direct electron transfer along the wire.

Structural superimposition of the air-oxidized and dithionite-reduced ACIII showed a main-chain RMSD of 0.4 Å (Fig. 2A), indicating that dithionite reduction does not induce obvious conformational changes at the current resolution. However, the difference map of ACIII (the air-oxidized map minus dithionite-reduced map) showed major electron potential differences at the periplasmic subunits (ActA, ActE, and ActB) and the cytoplasmic side of the TM region of ActA, ActC, and ActD (Fig. 2A). The increased electron potentials were observed at the six heme groups as well as the four iron-sulfur clusters (Fig. 2A and movie S3), indicating that these electron carriers are essentially reduced after dithionite treatment, which is consistent with the increased heme spectral differences upon dithionite reduction (fig. S1D).

The heme electron transfer wire in ActA and ActE subunits

ActA (Gln^{9}-Arg^{226}) and ActE (Cys^{33}-Asn^{193}) were found to be penta-heme and mono-heme subunits, respectively, which form the main electron transfer wire of the photosynthetic ACIII. ActA is membrane-anchored, with an N-terminal TM helix (α1, Gln^{9}-Trp^{43}). Five c-type hemes were bound in the loop regions between its six α helices on the periplasmic side (Fig. 2B). The C-terminal mono-heme binding domain of ActE is composed of three α helices and two turns (Fig. 2B), and our model showed a lipid anchor that is present at the N terminus of ActE (fig. S4D). This observation suggested the possibility that the consensus lipobox sequence L/V-A/T-G/A-C ($M^{30}TAC^{33}$) (fig. S6B) in the *actE* gene sequence may be excised from the transcript or degraded following translation in cells or at some point before the final complex assembly. This phenomenon was also observed in the respiratory ACIII (*17*).

The six heme groups bound by ActA and ActE are each covalently attached via thioester linkages to cysteine residues of highly conserved heme binding motifs (C-X-X-C-H), and their iron ions are axially coordinated through bi-His or His-Met residue couplets (Fig. 2C and fig. S6B). The five hemes of the ActA subunit are arranged in alternating parallel (heme_2,5 and heme_3,4) and perpendicular pairs (heme_2,3 and heme_4,5) (Fig. 2C). In particular, the heme_3,4 pair adopts typical stacked motif in van der Waals contact (edge-to-edge distance, 4.8 Å), whereas heme_2,3 (5.1 Å) and heme_4,5 (4.5 Å) exemplify the T-shaped heme pairs (Figs. 1D and 2C). The spatial organization of heme_2 to heme_5 resembles that of the tetraheme in *Shewanella oneidensis* STC, in which the electron transfer between stacked heme pairs is approximately an order of magnitude greater than for the T-shaped heme pairs (*25*). But the electronic coupling of T-shaped heme pairs would be strongly enhanced by cysteine linkages inserted in the space between these pairs (*26*). The heme_1 is closest in terms of edge-to-edge distance to [3Fe-4S] (8.3 Å), and it is buried in a hydrophobic pocket formed by residues from ActB, ActC, ActD, and ActE (fig. S6C). The porphyrin ring of the mono-heme in ActE is inclined about 60° compared to that of heme_5 in ActA, with an edge-to-edge distance of 9.0 Å and a center-to-center distance of 16.7 Å (Figs. 1D and 2C).

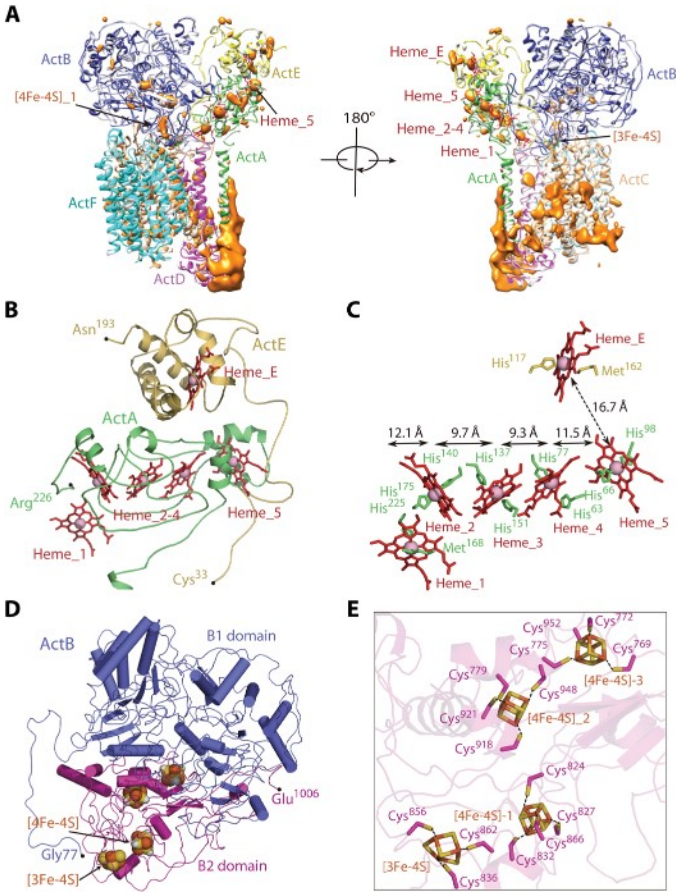

Fig. 2. Heme and iron-sulfur clusters in ActA and ActE subunits. (**A**) The air-oxidized minus dithionite-reduced electron potential difference map (orange) of the ACIII is shown from the front (left) and back (right) view. The structures of the air-oxidized and dithionite-reduced ACIII (white) are superimposed, with the iron-sulfur clusters and heme groups shown in sphere and stick models. The color code for each subunit and cofactors of the air-oxidized ACIII is the same as that in Fig. 1. (**B**) Ribbon representation of the ActA and ActE subunits bound with pentaheme and monoheme groups (red sticks). The N and C termini of the protein are highlighted with a black dot and labeled. (**C**) Spatial organization and immobilization of the pentaheme and monoheme groups in ActA and ActE subunits. The residues that axially coordinate the heme iron ions are shown as sticks and labeled; the center-to-center distances of the hemes are shown and labeled. (**D**) Overall structure of ActB subunit. The B1 and B2 domains are colored in blue and magenta, respectively. The iron-sulfur clusters are shown as spheres. (**E**) Coordination of the iron-sulfur clusters in the ActB subunit. The conserved cysteine residues that coordinate the iron-sulfur clusters are shown as sticks and labeled, and the B2 domain is shown as a ribbon with 80% transparency.

No midpoint redox potential data are available for the six hemes and iron sulfur clusters in *R. castenholzii* ACIII. The heme redox potentials of *R. marinus* ACIII was shown to range from −45 mV to +230 mV at neutral pH (*11*). Potentiometric titration of the c hemes in *F. johnsoniae* ACIII gives redox potentials at +331 mV and +439 mV (*18*). For *C. aurantiacus* ACIII, which shares 59% sequence identities with *R. castenholzii* ACIII, the heme midpoint redox potentials were determined to be −228 mV, −110 mV, +94 mV, and +391 mV (*8*). With the highest redox potential at +391 mV (*8*), the monoheme of ActE is believed to be the final electron prosthetic group to accept the electrons transferred from the five hemes in ActA. Regarding the high sequence homology and functional similarity (*9*) of ActA and ActE with that of *C. aurantiacus* and respiratory ACIIIs from *R. marinus* and *F. johnsoniae* (fig. S6, A to C), as well as the spatial distribution of the six hemes (Fig. 2, A to C), electrons can be sequentially transferred along a wire that begins with the heme_1 in ActA and ends with the monoheme in the ActE subunit, and then eventually to the acceptor auracyanin (*13*, *24*).

The iron-sulfur clusters bound in the ActB subunit

The largest subunit, ActB (Gly^{77}-Glu^{1006}), was found to be composed of 26 α helices and 17 β strands that can be divided into two subdomains: the B1 domain (Gly^{77}-Phe^{714}) and B2 iron-sulfur binding domain (Leu^{715}-Glu^{1006}) (Fig. 2D). The N terminus of ActB was resolved from Gly^{77}, just behind the signal peptidase cleavage site $A^{71}LA^{73}$. The twin-arginine translocase signal peptide assists with the translocation of ActB to periplasm (*27*). Superimposition analysis of ActB with PsrA and PsrB subunits of polysulfide reductase (PsrABC), an integral membrane-bound enzyme that performs quinone-coupled reduction of polysulfide substrates (*28*), revealed that the B2 iron-sulfur binding domain is similar to PsrB and that both the folding and positions of the four iron-sulfur clusters match well between the two subunits (fig. S7A). The analysis also revealed that the B1 domain of ActB forms a fold similar to the known substrate binding pocket of PsrA (fig. S9B), yet the absence of any cofactors in our model suggests that the function of ActB does not mirror the reduction activity of PsrA.

The four iron-sulfur clusters are covalently coordinated by conserved Cys residues (Fig. 2E and fig. S6D), with the largest edge-to-edge distance of 9.7 Å (Fig. 1D). The [3Fe-4S] is located at the interface with ActC and in the most proximity to the periplasmic side of the four-helix bundle that hosts the menaquinol binding pocket (Fig. 3A). This iron-sulfur cluster is the most probable primary electron acceptor from the menaquinol bound in the ActC subunit. The midpoint redox potential of [3Fe-4S] in *R. marinus* ACIII was determined to be +140 mV (*11*, *17*), which is sufficient for an uphill electron transfer from menaquinol (−70 mV at pH 7) (*29*). The role of the three [4Fe-4S] clusters in both respiratory and photosynthetic ACIIIs are still unknown. The air-oxidized minus dithionite-reduced electron potential differences at the [3Fe-4S] and three [4Fe-4S] clusters indicate that these iron-sulfur clusters can be reduced upon dithionite treatment (Fig. 2A and movie S3). An edge-to-edge distance of 8.3 Å was observed between the [3Fe-4S] and heme_1 in the ActC subunit (Fig. 1D), which suggests that the electrons accepted by the [3Fe-4S] cluster are most probably transferred along the heme wire to reduce a periplasmic electron carrier.

A menaquinol binding pocket located at the periplasmic side of ActC subunit

The ActC (Lys^{8}-Ala^{464}) and ActF (Gln^{4}-Ser^{399}) subunits each contain 10 TM helices. The middle eight helices are arranged into two four-helix bundles (TM2-5 and TM6-9 of ActC, and TM2′-5′ and TM6′-9′ of ActF), which were sandwiched by the intersection of TM1 (TM1′) and TM10 (TM10′) (Fig. 3A). The helix bundles of ActC and ActF resemble the structure of PsrC dimer (fig. S7C). Superimposition of the structures of ActC and PsrC gives a main-chain RMSD of 1.1 Å. The quinone binding pocket of PsrC, which is formed by the N-terminal four-helix bundle and located at the periplasmic side, was identified according to the structures complexed with MK-7, pentachlorophenol, and ubiquinone-1 (*28*).

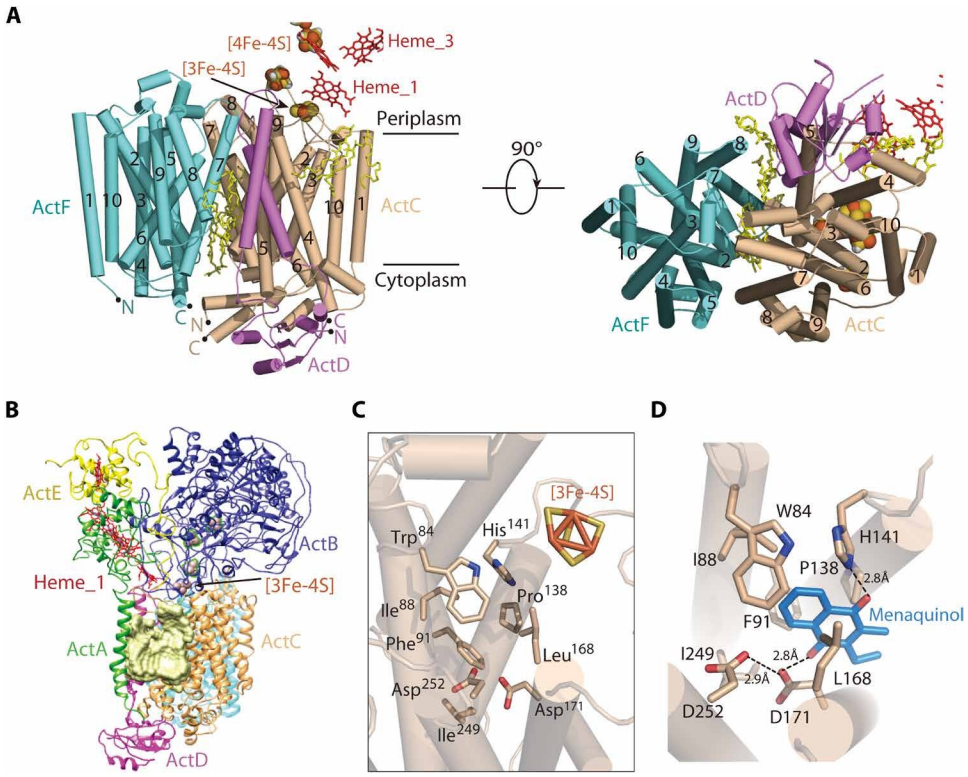

Fig. 3. TM region of R. castenholzii **ACIII and a putative menaquinol binding pocket.** (**A**) Ribbon representation of the side (left) and bottom-up (right) views of the ActC (wheat) and ActF (aquamarine) subunits. The TM helices of ActC and ActF are labeled with numbers, and the iron-sulfur clusters in ActB and heme groups in ActA subunit are shown in spheres and red sticks, respectively. The N and C termini of each subunit are highlighted with a black dot and labeled. (**B**) Open cavity (bright yellow) between the TM helices of ActA, ActC, and ActD subunits of ACIII, which is equivalent to the menaquinol binding pocket. The cavity inside the TM region of ACIII was calculated using the program HOLLOW (*44*), and it is shown as a surface model. (**C**) Zoomed-in view of the putative menaquinol binding pocket, with essential amino acids shown as stick models. (**D**) Interactions between the modeled menaquinol head (blue stick model) and the menaquinol binding pocket. Residues are shown as stick models, and the hydrogen bonding interactions are shown as dashed lines with distances labeled.

Although no menaquinol was found in the current structures, we observed an open cavity between the TM helices of ActA, ActD, and TM3/4 of ActC subunits, which is equivalent to the quinol binding pocket of PsrC (Fig. 3B and movie S4).

On the basis of structural analysis and comparison as well as sequence alignment (fig. S8), we identified a menaquinol binding pocket of ACIII at the periplasmic side of the first four-helix bundle in ActC, about 12 Å away from the [3Fe-4S] cluster (Fig. 3C). Adjacent to [3Fe-4S], a strictly conserved His^{141} residue replaces the Glu^{67} of PsrC quinol binding pocket (Fig. 3C and figs. S7D and S8), which is involved in proton transfer from the menaquinol (*30*). The side chains of Trp^{84}, Ile^{88}, Phe^{91}, Pro^{138}, and Leu^{168} further form a hydrophobic pocket that is capable of immobilizing the menaquinol head group (Fig. 3D). The two carbonyl oxygen atoms of the modeled menaquinol head are capable of forming hydrogen bonds with the imidazole group of His^{141} (2.8 Å) and the hydroxyl group of Asp^{171} (2.8 Å), which further forms hydrogen bonds with Asp^{252} (2.9 Å) (Fig. 3D). At the bottom of the pocket, Ile^{249} takes the position of Tyr^{130} in PsrC, which forms a hydrogen bond (2.6 Å) with the O1 carbonyl group of MK-7 (fig. S7D) (*28*). The menaquinol binding pocket of *R. castenholzii* ACIII shares high sequence homology and conformational similarity with that of *R. marinus* and *F. johnsoniae* ACIII (fig. S7, E and F), indicating that ACIIIs play essentially similar enzymatic function in the photosynthesis and respiration.

Putative proton translocation passages in the ActC and ActF subunits

On the basis of the structural comparison with the respiratory ACIII, we further identified a putative proton translocation passage in the ActC subunit. The passage begins at the cytoplasmic residues Arg^{198} and Asp^{199} and proceeds to the TM region located primarily at the first four-helix bundle of the periplasmic region (Fig. 4, A and C). This passage is composed of 22 proton-carrying residues that provide side chains for hydrogen bonding with protons (Fig. 4A). The air-oxidized minus dithionite-reduced electron potential differences were mainly distributed at the cytoplasmic side of TM1, TM3, TM4, TM5, and TM10 of ActC (Figs. 2A and 4C), where the menaquinol binding pocket and proton translocation passage are absent. Furthermore, we did not observe obvious structural differences at the proton translocation passage between the air-oxidized and dithionite-reduced structures (Fig. 2A).

In the middle of the passage, three strictly conserved residues—Arg^{394}, His^{246}, and His^{99}—form a hydrogen bonding network that links the menaquinol binding pocket and proton translocation passage (Fig. 4B). The imidazole group of His^{246} forms hydrogen bonds with the guanidine group of Arg^{394} (3.1 Å) and imidazole nitrogen of His^{99} (3.3 Å), which forms a weak hydrogen bond with the main chain of Ile^{95} (3.3 Å). The main-chain nitrogen of Ile^{95} is further hydrogen-bonded with the main-chain oxygen of Phe^{91} (3.1 Å), one of the key residues involved in menaquinol coordination. In close

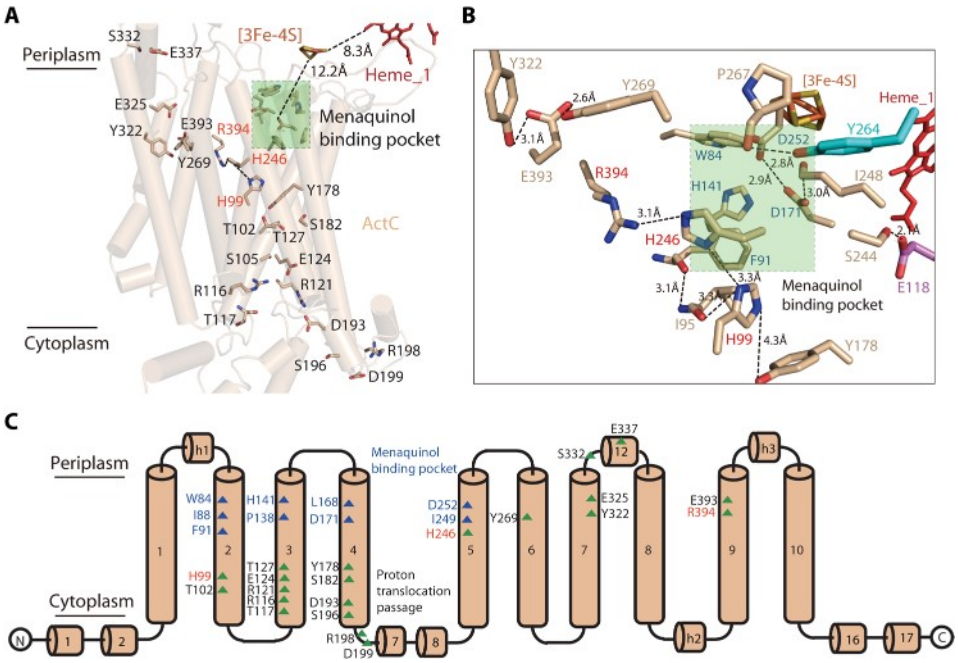

Fig. 4. Organization of the menaquinol binding pocket and proton translocation passage in the ActC subunit. (**A**) Organization of the menaquinol binding pocket (highlighted with a green box), [3Fe-4S] cluster, heme_1, and the putative proton translocation passage in ActC (wheat). The distance between [3Fe-4S] and the side chain of Asp^{171} in the menaquinol binding pocket is 12.2 Å, and the edge-to-edge distance between the [3Fe-4S] cluster and heme_1 is 8.3 Å. The residues that constitute the proton translocation passage and menaquinol binding pocket are shown as stick models, and the TM helices of ActC are shown as ribbon with 80% transparency. (**B**) Zoomed-in view of the hydrogen bonding networks between the menaquinol binding pocket and middle passage residues of the proton translocation passage in the ActC subunit, as well as the residues from the ActD and ActF subunits. Residues are shown as stick models, and the hydrogen bonding interactions are shown as dashed lines with distances labeled. (**C**) Topology diagram of the ActC subunit. The amino acids that constitute the menaquinol binding pocket and proton translocation pathway are shown in blue and green triangles, respectively.

proximity to His^{246}, Ile^{248} forms a hydrogen bond with Asp^{171} (3.0 Å), which is hydrogen-bonded with Asp^{252} (2.9 Å) at the top of the menaquinol binding pocket (Fig. 4B).

Arg^{394}, His^{246}, and His^{99} are strictly conserved in both the respiratory and photosynthetic ACIII (fig. S8). Superimposition analyses showed that the "triplet" residues adopt the same side-chain orientations and hydrogen bonding network as that from *R. marinus* and *F. johnsoniae* (Fig. 5, A and B), suggesting that these residues share a similar function in the respiratory and photosynthetic ACIII. Asp^{394} is also conserved in other polysulfide, tetrathionate, nitrate, and dimethyl sulfoxide reductases (*30*). Mutation of Arg^{394} in *Wolinella succinogenes* PsrC resulted in an inactive enzyme, which was suggested that it stabilizes the deprotonated quinol (*30*). Regarding the sequence conservation, location, and extensive hydrogen bonding interactions with the menaquinol binding pocket, the triplet residues are likely essential for coupling the menaquinol oxidation and proton translocation.

We observed a similar proton translocation passage in the ActF subunit formed by 20 less conserved amino acids (about 20% identities) from the cytoplasmic to periplasmic side (Fig. 5C and fig. S9). In the middle of the ActF passage, side chains of Glu^{335}, Ser^{217}, and Tyr^{339} are capable of forming hydrogen bonding interactions, but no menaquinol-binding pocket and similar hydrogen bonding networks as that in ActC were found (Fig. 5C). In addition, Ser^{217} and Tyr^{339} are less conserved in both the photosynthetic and respiratory ActF, and Glu^{335} is replaced by Arg in *C. aurantiacus* and His residue in the respiratory ActF (Fig. 5D and fig. S9). Minor electron potential differences were only observed at His^{287}, Ala^{189}, and Met^{65} of the ActF subunit, suggesting that this subunit is not sensitive to the air-oxidized and dithionite-reduced state of ACIII. To be noted, a conserved residue Tyr^{264F} forms a hydrogen bond with the main-chain oxygen of Pro^{267C} (2.8 Å), which is close to the periplasmic portion of the proton translocation passage in ActC (Fig. 4B). The distinct conservation of these proton translocation passages indicates that the ActC subunit plays consensus important role in both the respiratory and photosynthetic ACIII.

Extensive interactions between ActD and other subunits

The function of the ActD subunit in the ACIII remains obscure. We observed hydrogen bonding interactions between Asn^{100} of ActD and Tyr^{755} of ActB, as well as between Leu^{106} of ActD and Tyr^{753} of ActB (fig. S10A). We also observed extensive hydrophobic interactions between residues located in the ActD loop and subunits ActB, ActF, and ActC. These interactions can stabilize the conformation of TM5, which contributes to the menaquinol binding pocket (fig. S10A). Near the menaquinol binding pocket, a hydrogen bond is formed between the hydroxyl groups of Glu^{118} of ActD and Ser^{244} of ActC (2.1 Å), which was close to the His^{246} of ActC that would be essential for coupling the menaquinol oxidation and proton translocation (Fig. 4B). Thus, ActD might play a primary role in stabilizing the TM region of ACIII, which thereby contributes to a stable menaquinol binding pocket and proton translocation passage.

DISCUSSION

As a functional counterpart of the bc_1 complex, ACIII plays a central role in both the photosynthetic and respiratory ETC of a wide

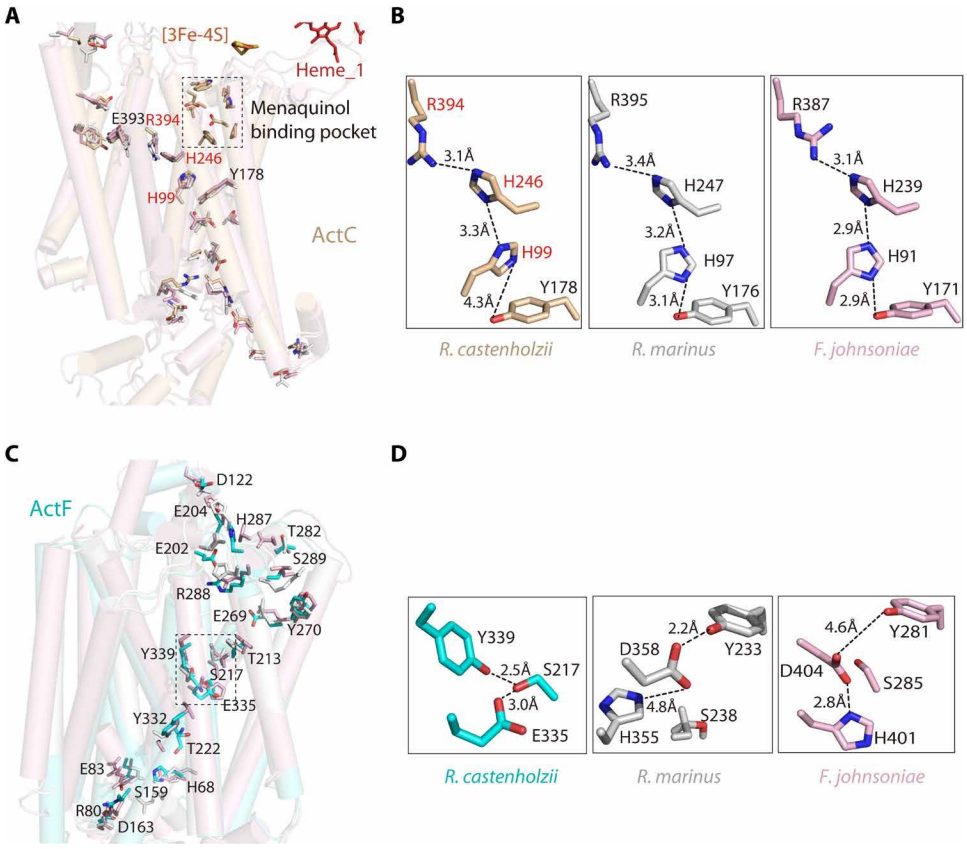

Fig. 5. Comparison of the proton translocation passages in the photosynthetic and respiratory ACIII. (**A**) Comparison of the proton translocation passage in *R. castenholzii* ActC (wheat) with that of the respiratory ActC from *R. marinus* (PDB 6f0k, white) and *F. johnsoniae* (PDB 6btm, pink). The [3Fe-4S] cluster, heme_1, and the amino acids are shown as sticks. (**B**) Middle passage residues that are capable of forming hydrogen bonding networks. (**C**) Putative proton translocation passage in *R. castenholzii* ActF subunit (aquamarine) and its superimposition with that of *R. marinus* (PDB 6f0k, white) and *F. johnsoniae* (PDB 6btm, pink). (**D**) The middle passage residues that are capable of forming hydrogen bonds in ActF subunits are shown in stick models.

range of bacterial taxa (*6*–*10*). It couples quinol oxidation with TM proton translocation to build up a TM proton gradient, which drives the formation of ATP required for bacterial growth. However, the nature of the coupling mechanism(s) for the respiratory and photosynthetic functions of ACIII has not been well discussed.

The photosynthetic bacterium *R. castenholzii* has evolved a simple but efficient cyclic ETC to transform solar energy into chemical energy that is different from the linear respiratory chain (*31*–*33*). Our study has revealed the structure of the first photosynthetic ACIII comprising six conserved subunits, in both the air-oxidized and dithionite-reduced states, as well as the nature and position of the cofactors, including six hemes and four iron-sulfur clusters. We also detected a menaquinol binding pocket positioned at the periplasmic side of the TM subunit ActC. This pocket is capable of immobilizing the menaquinol head group via strictly conserved residues (Fig. 3D), which is linked by extensive hydrogen bonding interactions with three proton-carrying residues in the middle of an apparent proton translocation passage. In addition, the ActD subunit is shown to coordinate extensive interactions with subunits ActA, ActB, ActC, and ActF.

Previous enzymatic analyses confirmed the activity of photosynthetic ACIII as a menaquinol:auracyanin or cyt c oxidoreductase (*9*). Recently, we revealed that *R. castenholzii* ACIII oxidizes menaquinol-4 or menaquinol-7 and transfers electrons to its periplasmic electron acceptor auracyanin (*24*). It has been revealed that there is a single quinol binding site in *R. marinus* ACIII by isothermal titration calorimetry experiments (*17*). The high sequence and structural similarity among photosynthetic and respiratory ACIIIs would also suggest a single menaquinol binding pocket of *R. castenholzii* ACIII. Within this pocket, menaquinol binds and is oxidized by the terminal electron acceptor auracyanin, releasing two protons into periplasm. Considering that menaquinone is reduced at the binding site of RC-LH complex (*23*), accepting two protons from cytoplasm, an apparent efficient quinone shuttling cycle is formed among RC-LH, the membrane quinone pool, and ACIII in the *R. castenholzii* simple cyclic photosynthetic ETC. As a result, with the reduction of one molecule menaquinone at RC-LH and the oxidation of one shuttled menaquinol at ACIII, two transferred electrons are accompanied with two protons transferred from cytoplasm to periplasm, yielding a H^+/e^- ratio of 2:2.

To date, no experimental data on the H^+/e^- stoichiometry for any ACIII were reported. Previous studies proposed that ACIII could also actively pump additional protons from cytoplasm into periplasm (*10*, *12*, *14*, *15*), which would yield a different H^+/e^- stoichiometry deduced from above quinone shuttling cycle. However, the detailed mechanism of its active proton translocation has not been elucidated. The lack of any redox-active cofactors in the TM and cytoplasmic regions of ACIII argues against a Q-cycle type

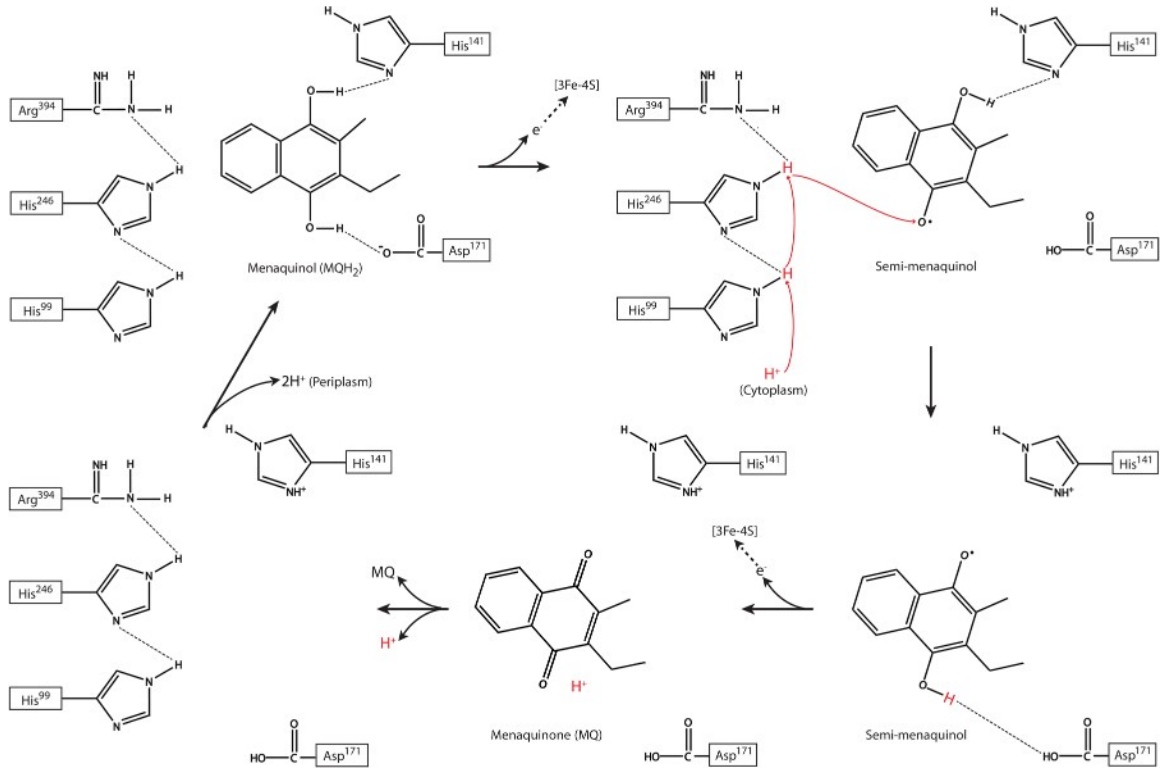

Fig. 6. Proposed redox-coupled proton translocation mechanism of the photosynthetic ACIII. The menaquinol head group and the side chains of the essential amino acids are shown to indicate the coupling mechanism of the photosynthetic ACIII from *R. castenholzii*. Upon menaquinol oxidation, two electrons are sequentially transferred to the [3Fe-4S] cluster with a time interval, two protons from oxidation of menaquinol are released to periplasmic space, and one proton is pumped from the cytoplasm (colored in red) through hydrogen bonding networking with the essential amino acids in the proton translocation passage. As a result, three protons are released into the periplasm per two electrons transferred during oxidation of one instance of menaquinol.

H^+ pumping mechanism, such as is used in the cyt bc_1 and *c*yt b_6f complexes.

A hypothesis of the redox-coupled proton translocation mechanism

Structural comparison and analyses revealed two putative proton translocation passages in ActC and ActF, respectively, for both photosynthetic and respiratory ACIII (Fig. 5, A and C). The side chains of the middle-passage triplet residues Arg^{394}, His^{264}, and His^{99} of ActC adopt exactly the same conformation for all three ACIIIs (Fig. 5B). However, the proton-carrying residues in the passage of ActF are less conserved than that of ActC (Fig. 5, C and D). Notably, the respiratory ACIIIs from *R. marinus* (*17*) and *F. johnsoniae* (*18*) contain two conserved His and Asp residues in the middle passage of ActF, but these two residues are replaced by Glu and Tyr in the *R. castenholzii* ACIII (Fig. 5D and fig. S9). In addition, neither menaquinol binding pocket nor hydrogen bonding network was found in ActF. Less differences of electron potential around ActF between the air-oxidized and dithionite-reduced states (Fig. 2A) suggest that ActF is insensitive to the changes of redox potential. Therefore, most probably, ActF passage lacks a driving force for efficient TM proton translocation. If there exists a redox-coupled active proton translocation in ACIII, it would be mostly located in the ActC subunit and driven by the coupling between menaquinol oxidation and putative proton passage, without the necessary conformational change.

On the basis of the above structural analysis and discussion, we propose a redox-coupled proton translocation mechanism for the photosynthetic ACIII, which occurs within the subunit of ActC (Fig. 6). In the menaquinol binding pocket, at the close-to-neutral pH environment (pH ~6.5) of periplasmic space, both Asp^{171} and His^{141} are deprotonated and coordinate the bound menaquinol (MQH_2) by hydrogen bonds. The hydroxyl hydrogens of menaquinol can be bound by the hydroxyl oxygen of Asp^{171} and imidazole nitrogen of His^{141}, respectively. Upon oxidation, the hydroxyl group of menaquinol that faces the side chain of Asp^{171} is first oxidized to form an intermediate semi-menaquinol. The released hydrogen protonates Asp^{171}. Lacking the coordination by Asp^{171}, the semi-menaquinol would be relocated in the binding pocket and thus enable extraction of one proton from the proximal proton passage of ActC, resulting in one proton translocated from the cytoplasm. The binding of the extracted proton will induce a reorganized electronic structure of semi-menaquinol, releasing another hydroxyl hydrogen to protonate His^{141}. The reorganized semi-menaquinol can be further coordinated by the hydroxyl group of Asp^{171}. Then, the semi-menaquinol is further oxidized to form menaquinone (MQ) and release the exacted proton. After the release of menaquinone and the extracted proton from the menaquinol binding pocket, the two protons from oxidation of menaquinol are released to periplasmic space with the deprotonation of Asp^{171} and His^{141}. During this proposed process, one instance of menaquinol oxidation is coupled to one proton pumped from the cytoplasm. As a result, three protons are released into the periplasm per two electrons transferred (Fig. 6).

The potential role of the [4Fe-4S] clusters

In both the respiratory and photosynthetic ACIII structures, a [3Fe-4S] cluster in the ActB subunit functions as the primary electron acceptor from menaquinol (*17*, *18*), donating the electrons along the six-heme wire and finally onto the periplasmic electron acceptor. Both the photosynthetic ACIII from *R. castenholzii* and the respiratory ACIII from *R. marinus* contain additional three [4Fe-4S] clusters, while only one [4Fe-4S] cluster was identified in the *F. johnsoniae* ACIII (*18*). The function of [4Fe-4S] clusters remains largely unknown.

Our observation of the electron potential differences of these [4Fe-4S] clusters between air-oxidized and dithionite-reduced states indicates that these clusters are either accessible to dithionite or connected to the electron transfer wire. In Psr with the absence of heme groups, two electrons released from MK-7 are transferred via five [4Fe-4S] clusters to the *bis*-MGD (bis-molybdopterin guanine dinucleotide) cofactor and then reduce polysulfide (*28*). Unfortunately, no cofactors were observed in the B1 domain of ActB subunit (fig. S7B), indicating an electron transfer dead end in these [4Fe-4S] clusters. How they contribute to the electron transfer of ACIII needs to be further considered.

Both heme and iron-sulfur cluster are single electron carriers that are unable to transfer two electrons simultaneously. Thus, a sequential transfer of electrons upon menaquinol oxidation is necessary. In addition, the latency time between the formation of semi-menaquinol and its further oxidation needs long enough to allow extraction of proton from the translocation passage, but it should not be too long to avoid the formation of reactive oxygen species. On the other side, the final periplasmic electron acceptor auracyanin can only accept one electron each time. Therefore, the speed of electron transfer in ACIII should be well controlled. The alternating T-shaped spatial organization of the six hemes in ACIII would limit in one order the electron transfer efficiency of the heme wire, which would increase the steady time of semi-menaquinol. This limitation could be further compensated by the [4Fe-4S] clusters playing as an electron sink. Overall, the possible electron transfer during menaquinol oxidation would look like that, the first electron would quickly sink into the [4Fe-4S] clusters via [3Fe-4S] with the formation of semi-menaquinol, and the second electron could then be transferred to the final periplasmic acceptor auracyanin via the heme wire; with a second auracyanin binding, the sinking electron in the [4Fe-4S] clusters could be further transferred to the final acceptor via the heme wire. As a result, the existence of the [4Fe-4S] clusters would be very important in assisting sequential and efficient transfer of two electrons with an intrinsic time interval.

In summary, our work provides a structural basis and conceptual insight into the coupling mechanism underlying menaquinol oxidation, electron transfer, and proton translocation for the photosynthetic ACIII, which seems likely to play the same role as a menaquinol: electron acceptor oxidoreductase in respiratory ACIIIs. Direct experimental will be required for definitive characterization the proton pumping mechanism of these ACIIIs.

MATERIALS AND METHODS

Extraction and purification of the photosynthetic ACIII from R. castenholzii

R. castenholzii DSM 13941 was grown in a batch culture anaerobically in modified PE medium at 50°C under high-light conditions for 10 days (*19*). Cells were harvested by centrifugation at 10,000*g* for 20 min, and the pellet was washed twice with 20 mM tris buffer (pH 7.4) and then stored at −40°C.

A suspension of whole membranes [with OD_{880} (optical density at 880 nm) = 20 cm^{-1}] in 20 mM tris-HCl (pH 8.0; buffer A) was treated with 1% β-octyl glucoside and stirred for 1 hour at room temperature in the dark. The extraction was centrifuged at 200,000*g* for 2 hours (Ti 70 rotor, 45,000 rpm) at 4°C. The pellets were resuspended in 50 mM sodium acetate (pH 5.0; buffer B) and treated with 0.5% β-dodecyl maltoside as above with 1% β-octyl glucoside. The supernatant from the second ultracentrifugation was collected and filtered through a 0.22-μm Millipore filter and subsequently loaded on a prepacked cation exchange chromatography column (SPHP5, GE Healthcare), which had been equilibrated with buffer B containing 0.04% β-dodecyl maltoside (which makes up buffer C). The column was extensively washed with 50 mM NaCl in buffer C until the eluent was colorless. Last, the crude ACIII was eluted from the column by a sodium gradient from 0.1 M NaCl to 0.4 M NaCl with 50 ml of buffer C at 2 ml min^{-1}. The collected fractions were concentrated and further purified by Superdex-200 gel filtration in buffer D [100 mM NaCl, 0.02% β-dodecyl maltoside, and 20 mM tris-HCl (pH 8.0)]. The fractions with an absorption ratio of A_{413}/A_{280} higher than 1.38 were pooled and used for cryo-EM analysis.

The polypeptide composition of the purified complex was determined by SDS-PAGE and blue-native PAGE. The sample solubility was optimized by dissolving samples in buffer containing 5% 2-mercaptoethanol for 30 min at 65°C; these conditions yielded the sharpest protein bands. The identity of SDS-PAGE and blue-native PAGE bands was confirmed by PMF using matrix-assisted laser desorption/ionization–time-of-flight (MALDI-TOF) mass spectroscopy.

PMF analysis of ACIII through MALDI-TOF mass spectroscopy

Stained bands from the SDS-PAGE were excised and destained and washed with 50% acetonitrile in 50 mM aqueous NH_4HCO_3. Proteins were then reduced with 10 mM dithiothreitol in 100 mM NH_4HCO_3 for 30 min. Cysteine residues in the proteins were further alkylated by 55 mM iodoacetamide in 100 mM NH_4HCO_3 for an additional 30 min. Trypsin (Promega Trypsin Gold, TPCK (L-1-tosylamido-2-phenylethyl chloromethyl ketone)–treated) in 50 mM NH_4HCO_3 was added to the gel pieces, and the enzymatic reaction proceeded overnight at 37°C. Afterward, peptides were extracted twice with 1% trifluoroacetic acid in 60% acetonitrile for 30 min. Extracted solutions were collected, dried completely in a speed-vac, and then redissolved in 50% acetonitrile containing 0.1% trifluoroacetic acid for mass spectrometry analysis.

The identities of proteins were determined by PMF using an ABI 4700 MALDI-TOF mass spectrometer. A mixture of the peptide sample and freshly prepared matrix solution (10 mg ml^{-1} α-cyano-4-hydroxycinnamic acid in 50% acetonitrile) was spotted on a stainless-steel target plate. Peptide mass value searches were performed against the National Center for Biotechnology Information (NCBI) database using Mascot software (www.matrixscience.com). The alkylation of cysteine was included as a possible modification. The mass tolerance for the monoisotopic peptide mass was set to ±0.6 Da.

Cryo–electron microscopy

Three-microliter aliquots of air-oxidized ACIII (4 mg ml^{-1}) was placed on the glow-discharged GiG R1.2/1.3 300-mesh gold holey carbon grid (Jiangsu Lantuo Biotechnology, China) and blotted for

3.0 s under a blot force of 1 at 100% humidity and 16°C before being flash-frozen in liquid ethane with a Mark IV Vitrobot system (FEI). Micrographs were acquired on a Titan Krios microscope (FEI) operated at 300 kV with a K2 Summit direct electron detector (Gatan). SerialEM (*34*) was used for automatic data collection. A nominal magnification of ×22,500 was used for imaging, which yielded a pixel size of 1.04 Å. The defocus range was between 1.2 and 3.3 μm. Each micrograph was dose-fractionated to 32 frames under a dose rate of 9.2 $e^-/Å^2$ per second and an exposure time of 6.4 s, which resulted in a total dose of about 59 $e^-/Å^2$.

For the sodium dithionite–reduced ACIII, 3-μl aliquots of a sample (4.5 mg ml^{-1}) were placed on the glow-discharged CryoMatrix R1.2/1.3 300-mesh amorphous alloy film (product no. M024-Au300-R12/13, Zhenjiang Lehua Technology Co. Ltd., China) and blotted for 3 s under a blot force of 0 at 100% humidity and 16°C before being flash-frozen in liquid ethane with a Mark IV Vitrobot system (FEI). Micrographs were acquired on a Titan Krios microscope (FEI) operated at 300 kV with a K2 Summit direct electron detector (Gatan). SerialEM was used for automatic data collection. A nominal magnification of ×22,500 was used for imaging, which yielded a pixel size of 1.04 Å. The defocus range was between 1.5 and 2.5 μm. Each micrograph was dose-fractionated to 32 frames under a dose rate of 9.4 $e^-/Å^2$ per second and an exposure time of 6.4 s, which resulted in a total dose of about 60 $e^-/Å^2$.

Image processing

Motion correction and exposure weighting was performed by the MotionCorr2 program (*35*), and the CTF (contrast transfer function) parameter was estimated using the Gctf program (*36*). The automatic particle picking was performed by Gautomatch (developed by K. Zhang, MRC Laboratory of Molecular Biology, Cambridge, UK) and Autopicking module in RELION; an initial model was made by e2initial model.py in EMAN2 software package (*37*), and all other steps were performed using RELION (*38*). For the air-oxidized ACIII dataset, 600 particles were manually picked and extracted for two-dimensional (2D) classification. The resulting 2D class averages were used as the templates for the automated particle picking, which yielded 257,815 particles from 1700 micrographs. The picked particles were extracted at 2 × 2 binning and subjected to three rounds of 2D classification. A total of 197,496 particles were finally selected for 3D classification.

Good 2D class averages in different orientations were selected to generate the initial model. A total of 177,489 particles were left after two rounds of 3D classification and re-extracted into the original pixel size of 1.04 Å. The following 3D refinement and postprocessing yielded an EM map with a resolution of 3.45 Å. After performing CTF refinement in RELION3, the resolution was increased to 3.24 Å. Reported resolutions were estimated with a soft-edge mask around the protein complex and micelle densities and based on the gold-standard FSC (Fourier Shell Correlation) = 0.143 criterion. Local resolution was estimated with Resmap (*39*).

For the reduced ACIII dataset, 1970 unscreened micrographs were subjected to 3D reference–based auto-picking in RELION3; reconstruction of the ACIII dataset was the 3D reference low pass–filtered to 20 Å. The resulting 488,581 particles were used to extract particles at 2 × 2 binning. After two rounds of 2D classification, 297,122 particles were selected for a 3D refinement and alignment-free 3D classification, and 219,913 particles from the best 3D class were re-extracted without downscaling. The following 3D refinement and postprocessing yielded an EM map with a resolution of 3.68 Å. CTF refinement and another alignment-free 3D classification improved the resolution to 3.51 and 3.46 Å, respectively. The final subset had 207,633 particles.

Model building, refinement, and validation

De novo atomic model building was conducted in Coot (*40*). Sequence assignments were guided by residues with bulky side chains. The starting models of the cofactors were taken from the CCP4 ligand library. The model was real space–refined by PHENIX (*41*, *42*) with intra-cofactor and protein-cofactor geometric constraints. The refinement and model statistics are listed in Table 1. All figures were prepared in PyMOL (www.pymol.org) or UCSF Chimera (*43*).

Calculation of the electron potential difference map

The difference map between air-oxidized and dithionite-reduced ACIII was calculated using EMAN2 (*37*). First, the cryo-EM map of dithionite-reduced ACIII was fitted to that of air-oxidized ACIII by Chimera and then was clipped into the same box size using "e2proc3d.py" in EMAN2. Then, the structural amplitudes of both maps were scaled using e2proc3d.py in EMAN2. Last, the difference map between the corrected maps was computed by the "e2.py" python tool in EMAN2 and further low-pass–filtered at a quarter of the Nyquist criterion.

SUPPLEMENTARY MATERIALS

Supplementary material for this article is available at http://advances.sciencemag.org/cgi/content/full/6/31/eaba2739/DC1

View/request a protocol for this paper from *Bio-protocol*.

REFERENCES AND NOTES

1. D. Xia, L. Esser, W. K. Tang, F. Zhou, Y. Zhou, L. Yu, C. A. Yu, Structural analysis of cytochrome bc1 complexes: Implications to the mechanism of function. *Biochim. Biophys. Acta* **1827**, 1278–1294 (2013).
2. D. Baniulis, E. Yamashita, H. Zhang, S. S. Hasan, W. A. Cramer, Structure-function of the cytochrome b6f complex. *Photochem. Photobiol.* **84**, 1349–1358 (2008).
3. J. L. Smith, H. Zhang, J. Yan, G. Kurisu, W. A. Cramer, Cytochrome bc complexes: A common core of structure and function surrounded by diversity in the outlying provinces. *Curr. Opin. Struct. Biol.* **14**, 432–439 (2004).
4. P. Mitchell, The protonmotive Q cycle: A general formulation. *FEBS Lett.* **59**, 137–139 (1975).
5. B. L. Trumpower, The protonmotive Q cycle. Energy transduction by coupling of proton translocation to electron transfer by the cytochrome bc1 complex. *J. Biol. Chem.* **265**, 11409–11412 (1990).
6. P. N. Refojo, F. L. Sousa, M. Teixeira, M. M. Pereira, The alternative complex III: A different architecture using known building modules. *Biochim. Biophys. Acta* **1797**, 1869–1876 (2010).
7. M. F. Yanyushin, M. C. del Rosario, D. C. Brune, R. E. Blankenship, New class of bacterial membrane oxidoreductases. *Biochemistry* **44**, 10037–10045 (2005).
8. X. Gao, Y. Xin, P. D. Bell, J. Wen, R. E. Blankenship, Structural analysis of alternative complex III in the photosynthetic electron transfer chain of Chloroflexus aurantiacus. *Biochemistry* **49**, 6670–6679 (2010).
9. X. Gao, Y. Xin, R. E. Blankenship, Enzymatic activity of the alternative complex III as a menaquinol:auracyanin oxidoreductase in the electron transfer chain of Chloroflexus aurantiacus. *FEBS Lett.* **583**, 3275–3279 (2009).
10. M. M. Pereira, P. N. Refojo, G. O. Hreggvidsson, S. Hjorleifsdottir, M. Teixeira, The alternative complex III from *Rhodothermus marinus*—A prototype of a new family of quinol:electron acceptor oxidoreductases. *FEBS Lett.* **581**, 4831–4835 (2007).
11. M. M. Pereira, J. N. Carita, M. Teixeira, Membrane-bound electron transfer chain of the thermohalophilic bacterium *Rhodothermus marinus*: A novel multihemic cytochrome bc, a new complex III. *Biochemistry* **38**, 1268–1275 (1999).
12. P. N. Refojo, M. A. Ribeiro, F. Calisto, M. Teixeira, M. M. Pereira, Structural composition of alternative complex III: Variations on the same theme. *Biochim. Biophys. Acta* **1827**, 1378–1382 (2013).

13. E. L. W. Majumder, J. D. King, R. E. Blankenship, Alternative complex III from phototrophic bacteria and its electron acceptor auracyanin. *Biochim. Biophys. Acta* **1827**, 1383–1391 (2013).
14. P. N. Refojo, M. Teixeira, M. M. Pereira, The alternative complex III of *Rhodothermus marinus* and its structural and functional association with caa_3 oxygen reductase. *Biochim. Biophys. Acta* **1797**, 1477–1482 (2010).
15. P. N. Refojo, M. Teixeira, M. M. Pereira, The alternative complex III: Properties and possible mechanisms for electron transfer and energy conservation. *Biochim. Biophys. Acta* **1817**, 1852–1859 (2012).
16. M. F. Yanyushin, Fractionation of cytochromes of phototrophically grown *Chloroflexus aurantiacus*. Is there a cytochrome bc complex among them? *FEBS Lett.* **512**, 125–128 (2002).
17. J. S. Sousa, F. Calisto, J. D. Langer, D. J. Mills, P. N. Refojo, M. Teixeira, W. Kühlbrandt, J. Vonck, M. M. Pereira, Structural basis for energy transduction by respiratory alternative complex III. *Nat. Commun.* **9**, 1728 (2018).
18. C. Sun, S. Benlekbir, P. Venkatakrishnan, Y. Wang, S. Hong, J. Hosler, E. Tajkhorshid, J. L. Rubinstein, R. B. Gennis, Structure of the alternative complex III in a supercomplex with cytochrome oxidase. *Nature* **557**, 123–126 (2018).
19. S. Hanada, S. Takaichi, K. Matsuura, K. Nakamura, *Roseiflexus castenholzii* gen. nov., sp. nov., a thermophilic, filamentous, photosynthetic bacterium that lacks chlorosomes. *Int. J. Syst. Evol. Microbiol.* **52**, 187–193 (2002).
20. R. E. Blankenship, Early evolution of photosynthesis. *Plant Physiol.* **154**, 434–438 (2010).
21. B. K. Pierson, R. W. Castenholz, A phototrophic gliding filamentous bacterium of hot springs, *Chloroflexus aurantiacus*, gen. and sp. nov. *Arch. Microbiol.* **100**, **5**, 24 (1974).
22. M. Yamada, H. Zhang, S. Hanada, K. V. P. Nagashima, K. Shimada, K. Matsuura, Structural and spectroscopic properties of a reaction center complex from the chlorosome-lacking filamentous anoxygenic phototrophic bacterium *Roseiflexus castenholzii*. *J. Bacteriol.* **187**, 1702–1709 (2005).
23. Y. Xin, Y. Shi, T. Niu, Q. Wang, W. Niu, X. Huang, W. Ding, L. Yang, R. E. Blankenship, X. Xu, F. Sun, Cryo-EM structure of the RC-LH core complex from an early branching photosynthetic prokaryote. *Nat. Commun.* **9**, 1568 (2018).
24. C. Wang, Y. Xin, Z. Min, J. Qi, C. Zhang, X. Xu, Structural basis underlying the electron transfer features of a blue copper protein auracyanin from the photosynthetic bacterium *Roseiflexus castenholzii*. *Photosynth. Res.* **143**, 301–314 (2020).
25. J. H. van Wonderen, C. R. Hall, X. Jiang, K. Adamczyk, A. Carof, I. Heisler, S. E. H. Piper, T. A. Clarke, N. J. Watmough, I. V. Sazanovich, M. Towrie, S. R. Meech, J. Blumberger, J. N. Butt, Ultrafast light-driven electron transfer in a Ru(II)tris(bipyridine)-labeled multiheme cytochrome. *J. Am. Chem. Soc.* **141**, 15190–15200 (2019).
26. X. Jiang, B. Burger, F. Gajdos, C. Bortolotti, Z. Futera, M. Breuer, J. Blumberger, Kinetics of trifurcated electron flow in the decaheme bacterial proteins MtrC and MtrF. *Proc. Natl. Acad. Sci. U.S.A.* **116**, 3425–3430 (2019).
27. T. Palmer, B. C. Berks, The twin-arginine translocation (Tat) protein export pathway. *Nat. Rev. Microbiol.* **10**, 483–496 (2012).
28. M. Jormakka, K. Yokoyama, T. Yano, M. Tamakoshi, S. Akimoto, T. Shimamura, P. Curmi, S. Iwata, Molecular mechanism of energy conservation in polysulfide respiration. *Nat. Struct. Mol. Biol.* **15**, 730–737 (2008).
29. B. Schoepp-Cothenet, C. Lieutaud, F. Baymann, A. Vermeglio, T. Friedrich, D. M. Kramer, W. Nitschke, Menaquinone as pool quinone in a purple bacterium. *Proc. Natl. Acad. Sci. U.S.A.* **106**, 8549–8554 (2009).
30. W. Dietrich, O. Klimmek, The function of methyl-menaquinone-6 and polysulfide reductase membrane anchor (PsrC) in polysulfide respiration of *Wolinella succinogenes*. *Eur. J. Biochem.* **269**, 1086–1095 (2002).
31. A. M. Collins, Y. Xin, R. E. Blankenship, Pigment organization in the photosynthetic apparatus of *Roseiflexus castenholzii*. *Biochim. Biophys. Acta* **1787**, 1050–1056 (2009).
32. Y. Tsukatani, N. Nakayama, K. Shimada, H. Mino, S. Itoh, K. Matsuura, S. Hanada, K. V. P. Nagashima, Characterization of a blue-copper protein, auracyanin, of the filamentous anoxygenic phototrophic bacterium *Roseiflexus castenholzii*. *Arch. Biochem. Biophys.* **490**, 57–62 (2009).
33. E. L.-W. Majumder, J. D. Olsen, P. Qian, A. M. Collins, C. N. Hunter, R. E. Blankenship, Supramolecular organization of photosynthetic complexes in membranes of *Roseiflexus castenholzii*. *Photosynth. Res.* **127**, 117–130 (2016).
34. D. N. Mastronarde, Automated electron microscope tomography using robust prediction of specimen movements. *J. Struct. Biol.* **152**, 36–51 (2005).
35. S. Q. Zheng, E. Palovcak, J.-P. Armache, K. A. Verba, Y. Cheng, D. A. Agard, MotionCor2: Anisotropic correction of beam-induced motion for improved cryo-electron microscopy. *Nat. Methods* **14**, 331–332 (2017).
36. K. Zhang, Gctf: Real-time CTF determination and correction. *J. Struct. Biol.* **193**, 1–12 (2016).
37. G. Tang, L. Peng, P. R. Baldwin, D. S. Mann, W. Jiang, I. Rees, S. J. Ludtke, EMAN2: An extensible image processing suite for electron microscopy. *J. Struct. Biol.* **157**, 38–46 (2007).
38. S. H. W. Scheres, RELION: Implementation of a Bayesian approach to cryo-EM structure determination. *J. Struct. Biol.* **180**, 519–530 (2012).
39. A. Kucukelbir, F. J. Sigworth, H. D. Tagare, Quantifying the local resolution of cryo-EM density maps. *Nat. Methods* **11**, 63–65 (2013).
40. P. Emsley, K. Cowtan, Coot: Model-building tools for molecular graphics. *Acta Crystallogr. D Biol. Crystallogr.* **60**, 2126–2132 (2004).
41. P. D. Adams, P. V. Afonine, G. Bunkóczi, V. B. Chen, I. W. Davis, N. Echols, J. J. Headd, L.-W. Hung, G. J. Kapral, R. W. Grosse-Kunstleve, A. J. M. Coy, N. W. Moriarty, R. Oeffner, R. J. Read, D. C. Richardson, J. S. Richardson, T. C. Terwilliger, P. H. Zwart, PHENIX: Acomprehensive Python-based system for macromolecular structure solution. *Acta Crystallogr. D Biol. Crystallogr.* **66**, 213–221 (2010).
42. P. V. Afonine, J. J. Headd, T. C. Terwilliger, P. D. Adams, New tool:phenix.real_space_refine. *Comput. Crystallogr. Newslett.* **4**, 43–44 (2013).
43. T. D. Goddard, C. C. Huang, T. E. Ferrin, Visualizing density maps with UCSF Chimera. *J. Struct. Biol.* **157**, 281–287 (2007).
44. B. K. Ho, F. Gruswitz, HOLLOW: Generating accurate representations of channel and interior surfaces in molecular structures. *BMC Struct. Biol.* **8**, 49 (2008).

Acknowledgments: We thank W. Tang, S. Min, and J. Qi at Hangzhou Normal University for their assistance in sample preparation and biochemical analyses. We would also like to thank P. Shan and R. Su at F.S. laboratory for their assistances. The EM works were performed at Center for Biological Imaging (CBI; http://cbi.ibp.ac.cn), Institute of Biophysics, Chinese Academy of Sciences and Hangzhou Normal University. We also thank S. Chang in the Center of Cryo-Electron Microscopy (CCEM), Zhejiang University for their technical assistance on cryo-EM studies. **Funding:** This work was supported by grants from the National Natural Science Foundation of China (31570738, 31870740, and 31400630) to X.X. and by grants from Chinese Academy of Sciences (XDB08030202) and Ministry of Science and Technology of China (2017YFA0504700) to F.S. **Author contributions:** X.X., Y.X., and F.S. initiated the project and supervised all experiments. Y.X. and C.W. isolated and purified the photosynthetic ACIII from *R. castenholzii*. Y.S. and C.W. performed single-particle cryo-EM grid preparation, data collection, image processing, and all model building and refinement. Y.X. and C.W. performed spectroscopic and mass spectrometry analyses of the ACIII. Y.S., R.E.B., F.S., and X.X. analyzed the data and wrote the manuscript. **Competing interests:** The authors declare that they have no competing interests. **Data and materials availability:** Cryo-EM maps and atomic coordinates of the air-oxidized and dithionite-reduced photosynthetic ACIII have been deposited into the Electron Microscopy Data Bank (accession codes, EMD-0937 and EMD-0936) and the Protein Data Bank (PDB) (accession codes, 6LOE and 6LOD), respectively. All data needed to evaluate the conclusions in the paper are present in the paper and/or the Supplementary Materials. Additional data related to this paper may be requested from the authors.

Submitted 3 January 2020
Accepted 11 June 2020
Published 29 July 2020
10.1126/sciadv.aba2739

Citation: Y. Shi, Y. Xin, C. Wang, R. E. Blankenship, F. Sun, X. Xu, Cryo-EM structures of the air-oxidized and dithionite-reduced photosynthetic alternative complex III from *Roseiflexus castenholzii*. *Sci. Adv.* **6**, eaba2739 (2020).